https://doi.org/10.1016/j.jfluidstructs.2018.09.013 [1]

Numerical and experimental study on the drainage and collapse of a floating flexible bag structure

D. Kristiansen, B. Su, Z. Volent

SINTEF Ocean, Trondheim, Norway

Abstract

This paper addresses the possible drainage and collapse of closed flexible cages in sea-based fish farming. A closed flexible cage is a floating bag structure containing water that is enclosed from the ambient water. Possible density stratification in typical fjord locations can cause buoyancy driven discharge from the containment if damages occur under special operational conditions. The discharge may in turn cause drainage and collapse of the closed flexible cage. A combined structural and hydrodynamic model was developed to study the process of drainage and collapse of a floating closed flexible bag structure. Scaled physical model experiments with buoyancy-driven drainage of a hemispherical bag structure was conducted and compared with results from numerical simulations. Good comparison was observed for the flexible deformations and the drainage time. Main characteristics of the drainage process and performance of the numerical model are discussed. Implications from the present results on the design of closed flexible cages are suggested. To the best of the authors' knowledge, the present study is the first to consider the drainage and collapse of a floating flexible bag containment structure through both numerical and experimental methods.

Keywords: Hydroelasticity, Finite Element Method, Fluid-structure interaction, Closed cages, Discharge, Drainage

1. Introduction

Floating closed containment structures for fish farming, referred to as closed cages, are structures containing a water volume for fish production

that is enclosed from the ambient water. From a marine technology perspective, closed cages are novel structures where the contained water accounts for the major part of the structures displacement. Closed cages are gaining new attraction as an alternative to open net-based structures for sea-based farming of Atlantic salmon in Norway. There are several reasons for this. One motivation for use of closed cages in farming of Atlantic salmon is to improve the fish health and welfare and thus the farming efficiency by having better control of water quality of the contained water, by means of water temperature, amount of dissolved oxygen, acidity and more. A controllable water exchange system is then needed, compared to traditional net-based fish-farm structures where water exchange is governed by natural convection through the net. The risk of parasite infections (sea-lice) in closed cages is reduced relative to open net-cages by pumping inlet water from water depths of about 20 meters or more. Further, farming in closed cages makes is possible to collect waste and deposits resulting from the production, such that the negative impact on the local environment is reduced. Several types of closed cages exist with various structural properties, ranging from rigid concrete structures to highly flexible bag structures made of fabric. When fabric is used as construction material for marine applications, effects of hydroelasticity are important to consider (Løland and Aarsnes (1994)). Hydroelasticity is the mutual dependency between hydrodynamic loads and flexible deformations of the structure. Hydroelastic theories for modeling of the global response of marine structures were reviewed by Chen et al. (2006) and Korobkin et al. (2011). Design aspects of flexible closed-cage structures were presented by Solaas et al. (1993), discussing different scenarios with hydrostatic pressure differences between the inside and the outside of the bag and how this affects the shape and flexible properties of the structure. Hydrostatic pressure differences can be due to the filling level in the containment, or due to differences in water density between the contained water and the ambient. The behaviour of closed flexible cages subjected to a steady current was studied in scaled physical model experiments by Lader et al. (2015) and Strand et al. (2016). Several filling ratios were tested, where the current induced deformations and drag forces were found to increase largely for lower fill ratios. Scaled physical model experiments were also conducted to investigate the behavior of closed flexible cages in waves (Lader et al. (2017)). Complex deformations and dynamic motions of the bag structure were observed for lower fill ratios. This is also supported by experiences in the field from operators of closed flexible cages, and why an internal excess pressure is usually applied by over-filling of the cage. Difference in water level between the inside and the outside is by operators reported to be up to the order 0.1 m. The internal excess pressure will cause discharge of contained water if a damage

with a hole in the bag occurs. Depending on the net volume in-flux from the water exchange system of the cage, such discharge may cause drainage of the bag structure. Drainage can be critical for closed flexible cages used for fish farming. If a closed flexible cage begins to drain, reduction of the cage volume will increase the effective stocking density inside the cage. If the stocking density becomes too high, the fish health might be at risk due to lack of oxygen or crushing at extreme cases. Development of numerical methods and computational models for simulating the mutual interaction of fluid flows and complex structural deformations (FSI) is a hot research topic with many applications. Numerical models based on computational fluid dynamics (CFD) methods solving the equations of motion for the fluid flow can be powerful tools with possibility to handle flows in complex geometries and interaction with flexible structures (see e.g. Hart et al. (2003) and Griffith et al. (2009)). A review of numerical methods for fluid structure interaction was presented by Hou et al. (2012). Use of CFD methods require that the volume occupied by the fluid and time interval of interest is discretized with a computational grid in space-time, where the grid resolution must be sufficient to resolve the physics of the flow. Turbulence models are often applied to account for flow effects from unresolved (sub-grid) scales to keep the computational cost at an acceptable level. However, the temporal and spatial resolutions are interdependent through numerical stability criteria, which can make the numerical solution to flow problems involving multiple scales challenging. Numerical methods for multi-scale and multi-resolution problems is a developing research field with many applications (see e.g. Weinan and Engquist (2003)).

This paper addresses the process of drainage and collapse of a floating flexible bag structure caused by discharge of contained water when the density of the contained water is larger than the ambient water density. This has relevance for closed flexible cages used for farming of Atlantic salmon at fjord locations where density stratification can occur. A numerical simulation model is developed to study the fluid-structure interaction problem, which combines a dynamic model for the structure with simplified hydrodynamic models. The drainage process is studied by means of scaled physical model tests and numerical simulations with the numerical model presented. To the best of the authors' knowledge, the present study is the first to consider the drainage and collapse of a floating flexible bag containment structure through both numerical and experimental methods.

2. Material and Methods

Numerical modeling and simulation of the drainage and collapse of a floating flexible bag structure is challenging due to large differences in spatial and temporal scales of the flow, combined with large and complex structural deformations. Although advanced computational methods for modeling of multi-scale problems and complex fluid-structure interactions might be applied to address the present problem (see section 1), we will here make use of simplified rational models to obtain a dedicated simulation tool for the study of drainage and collapse of floating closed flexible bags.

2.1. Numerical simulation framework

The time-domain simulation tool FhSim (see Reite et al. (2014)) is used as the simulation framework for system assimilation, time integration and visualization of the numerical model system. FhSim is mainly a software tool for solving mathematical models based on Ordinary Differential Equations (ODEs) in the time domain. Model development in FhSim is modular, where complex systems are modeled as a collection of interconnected sub-models. In the present study, a new sub-model is developed in FhSim to simulate drainage of closed flexible cages, which includes a Finite Element (FE) based structural model combined with simplified hydrodynamic models.

2.2. Structural model

A finite element model, based on the so-called rotation-free (RF) shell elements, is developed for simulating structural deformation of closed flexible cage. The RF shell element requires only translational degrees of freedom at the mesh nodes, by which the complication of nonlinear formation of large rotations can be avoided. This rotation-free formulation greatly saves on computational cost due to the significant reduction in the number of degrees of freedom, thereby it is well suited for the present study where we need to handle large structural deformations and long-time simulations of fluid-structure interaction.

The RF shell elements belong to the family of flat shell elements formed by the superposition of a membrane element and a plate bending element. The strain energy, U, is expressed as the superposition of the energies due to the membrane and bending strains:

$$U = U_m + U_b = \int \frac{1}{2} \boldsymbol{\varepsilon}_m^T \boldsymbol{\sigma}_m \mathrm{d}V + \int \frac{1}{2} \boldsymbol{\varepsilon}_b^T \boldsymbol{\sigma}_b \mathrm{d}V \tag{1}$$

For linearly elastic materials, the relation between stresses, σ, and strains, ε, is given by Hooke's law:

$$\boldsymbol{\sigma} = \mathbf{E}\boldsymbol{\varepsilon} \tag{2}$$

where the constitutive matrix for thins shells, using the assumption of plane stress, is

$$\mathbf{E} = \frac{\mathrm{E}}{1-\nu^2}\begin{bmatrix} 1 & \nu & 0 \\ \nu & 1 & 0 \\ 0 & 0 & \frac{1-\nu}{2} \end{bmatrix} \tag{3}$$

where E is the Young's modulus, is the Poisson's ratio. The linear membrane strains, $\boldsymbol{\varepsilon}_m$, are

$$\boldsymbol{\varepsilon}_m = \begin{Bmatrix} \varepsilon_x \\ \varepsilon_y \\ \gamma_{xy} \end{Bmatrix} = \begin{Bmatrix} \frac{\partial u}{\partial x} \\ \frac{\partial v}{\partial y} \\ \frac{\partial u}{\partial y} + \frac{\partial v}{\partial x} \end{Bmatrix} \tag{4}$$

where u and v are the in-plane displacements. Thin plates are described by Kirchhoff's plate theory, with bending strains

$$\boldsymbol{\varepsilon}_b = z\boldsymbol{\kappa} = z\begin{Bmatrix} \kappa_{xx} \\ \kappa_{yy} \\ \kappa_{xy} \end{Bmatrix} = z\begin{Bmatrix} -\frac{\partial^2 w}{\partial x^2} \\ -\frac{\partial^2 w}{\partial y^2} \\ -2\frac{\partial^2 w}{\partial x \partial y} \end{Bmatrix} \tag{5}$$

where w is the out-of-plane displacement and $\boldsymbol{\kappa}$ is a generalized curvature field. In FE calculations, $\boldsymbol{\varepsilon}_m$ and $\boldsymbol{\kappa}$ are interpolated from the element degrees of freedom (DOF), $\mathbf{d}$, as

$$\boldsymbol{\varepsilon}_m = \mathbf{B_m d} \tag{6}$$

$$\boldsymbol{\kappa} = \mathbf{B_d d} \tag{7}$$

Compared to conventional shell formulations the RF shell elements do not include any rotational DOF. Instead, constant curvatures are approximated from the out-of-plane displacements of a patch of usually four triangular elements. Figure 1 shows a patch of the three-node triangle elements. The nodes 1, 2, and 3 in the main central triangle (M) are marked with circles while the external nodes in the patch (nodes 4, 5 and 6) are marked with squares. Mid-side points in the central triangle are also marked with smaller squares. The curvature within the central triangle can be expressed in terms of a constant assumed curvature field as:

$$\boldsymbol{\kappa} = \frac{1}{A_M}\oint \begin{bmatrix} -n_x & 0 \\ 0 & -n_y \\ -n_y & -n_x \end{bmatrix} \begin{Bmatrix} \frac{\partial w}{\partial x} \\ \frac{\partial w}{\partial y} \end{Bmatrix} \mathrm{d}\Gamma = \mathbf{B_b w} \tag{8}$$

where A_M is the area of the central triangle in Figure 1, Γ is the boundary of the central triangle and $\mathbf{n} = (\mathbf{n_x}, \mathbf{n_y})$ is the boundary normal, $\mathbf{w} =$

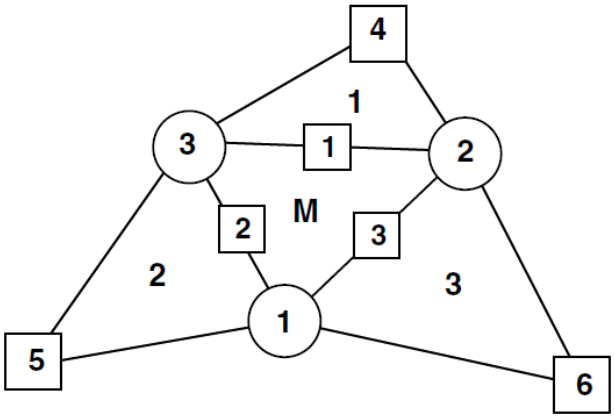

Figure 1: Patch of three-node triangular elements including the central triangle (M) and three adjacent triangles (1, 2, 3) (Courtesy: Flores and Oate (2005)).

$[\mathbf{w_1}, \mathbf{w_2}, \mathbf{w_3}, \mathbf{w_4}, \mathbf{w_5}, \mathbf{w_6}]$ are the out-of-plane displacements of the six nodes of the four-element patch linked to the element M, the expression of the 3×6 $\mathbf{B_b}$ matrix can be found, for example, in Onate and Cervera (1993).

The plate bending moments are related to the curvatures by the standard constitutive equations:

$$\mathbf{m} = \left\{ \begin{array}{c} M_{xx} \\ M_{yy} \\ M_{xy} \end{array} \right\} = \mathbf{D_b} \boldsymbol{\kappa} \tag{9}$$

$$\mathbf{D_b} = \frac{t^3}{12} \mathbf{E} \tag{10}$$

where t is the plate thickness.

Substituting the resulting expressions of stresses and strains into Eq. (1), the element tangent stiffness matrix becomes

$$\mathbf{K} = \mathbf{K_m} + \mathbf{K_b} = \int t \mathbf{B_m^T} \mathbf{E} \mathbf{B_m} \mathrm{d}A + \int \mathbf{B_b^T} \mathbf{D_b} \mathbf{B_b} \mathrm{d}A \tag{11}$$

where $\mathbf{K_m}$ and $\mathbf{K_b}$ are the contributions from the membrane part and the plate bending part, respectively.

The main merits of the RF shell elements expressed above are the reduction in the number of DOF and, for nonlinear formulations, the absence of all the difficulties related to large rotations. The total number of DOF necessary to obtain a certain accuracy is found to be less than half for an RF element compared to the corresponding elements that use rotational DOF, for many benchmark examples (see e.g. Sabourin and Brunet (2006) and Flores and

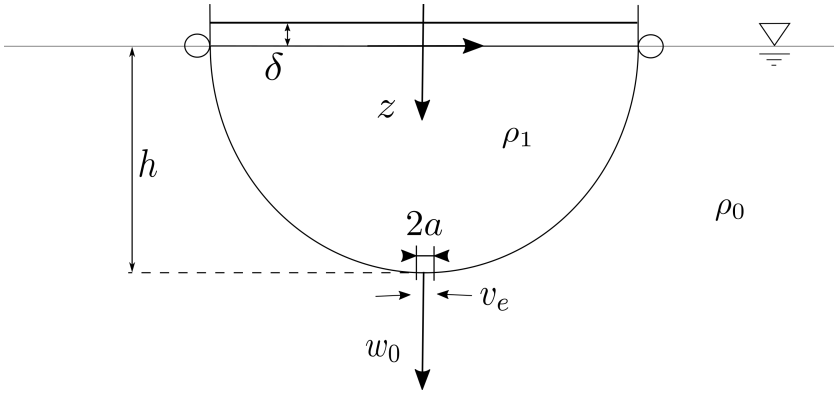

Figure 2: Definition of model dimensions and parameters of the hydrodynamic discharge model for the floating bag structure.

Oate (2007)). However, it is also found that the plate bending parts of most RF shell formulations are sensitive to element shape distortion (Gärdsback and Tibert (2007)). A consequence of this is that the accuracy of most RF shell elements is unsatisfactory for unstructured meshes.

In the present numerical study, a RF shell formulation introduced by Onate and Cervera (1993) and further developed by Flores and Oate (2005) was implemented. Considering that the RF shell formulation is sensitive to element shape distortion, structured meshes were used in all simulations.

2.3. Discharge hydrodynamic model

A hydrodynamic model for the discharge of contained water is developed from potential flow theory. Due to a higher water density inside the containment compared to the outside, there is a hydrostatic pressure difference between the inside and the outside of the closed containment. Typically, there is also a higher water level δ inside the containment compared to the outside. Parameters of the discharge model for the floating bag structure are defined in Fig. 2. The hydrostatic pressure p_0 and p_1 for the external and contained water, respectively, at a given vertical position $z = h$, is

$$p_0(h) = \int_0^h \rho_0(z) g \mathrm{d}z \,, \qquad p_1(h) = \int_{-\delta}^h \rho_1(z) g \mathrm{d}z \tag{12}$$

where g is the acceleration of gravity, $\rho_0(z)$ and $\rho_1(z)$ are the density profiles of the ambient water and contained water, respectively. We consider the case of a uniform density ρ_1 inside and ρ_0 outside the containment, where $\rho_1 > \rho_0$. Then the hydrostatic pressure difference is

$$\Delta p(z) = p_1(z) - p_0(z) = (\rho_1 - \rho_0) g z + \rho_1 g \delta \tag{13}$$

This pressure difference implies a force on the bag structure, but more important, it may cause discharge of water from the containment system in a damage situation with a hole in the membrane structure. This can in turn lead to drainage and collapse of the structure. Buoyancy driven flows are characterized by the densimetric Froude number

$$\mathrm{Fn} = \frac{U}{\sqrt{\hat{g}L}} \tag{14}$$

where U is characteristic velocity, $\hat{g} = g((\rho_1 - \rho_0))/\rho_1$ is called the reduced gravity and L is a characteristic length (Turner 1979). For the given problem, the largest difference in hydrostatic pressure appears at the deepest point of the containment, where a damage would be most critical in terms of drainage speed. Hence, we will in the following consider the case of a circular opening at the bottom pole of the hemispherical flexible bag.

In the following, an expression for the discharge velocity will be established. The jump in hydrostatic pressure through the opening at the bottom of the containment will cause discharge of water from the containment into the surroundings. The flow exterior to the opening appear as a forced plume. Forced plumes are driven both by discharge of momentum and buoyancy, where the limiting cases are non-buoyant jets and pure plumes (Morton (1959)). Observations of jets and plumes shows that there is an increasing vertical flow with depth, which implies a mean inflow across the boundary of the jet from the surroundings. In other words, fluid is entrained from the surroundings to maintain the flow. The entrainment velocity v_e is defined as the transversal speed at the boundary of the plume/jet. According to Batchelor (1954) the entrainment velocity for non-buoyant jets and pure plumes has a linear relation to the plume/jet centre velocity w_m expressed as $v_e = \alpha w_m$, where α is the entrainment constant. For a pure non-buoyant axisymmetric jet, $\alpha = 0.031$, while $\alpha = 0.041$ for an axisymmetric plume (Blevins (2003)).

The external flow outside the jet can be described by the Bernoulli equation:

$$-\rho\frac{\partial\phi}{\partial t} + \frac{1}{2}\rho|V|^2 + p - \rho g z = c \tag{15}$$

where c is an arbitrary constant. If we consider the steady flow after the transient start-up of the drainage process, a quasi-static approach can be used to find an expression for the external pressure at damage location. Assume the damage is located at depth $z = h$. Steady flow means we can neglect the first term on the left hand side of Eq. (15). Just outside the jet the fluid velocity V is horizontal and equal to the entrainment velocity v_e (cf. Fig. 2). By setting the constant $c = 0$, we obtain the following expression

for the total external pressure at the opening, just outside the jet:

$$p = -\frac{1}{2}\rho_0|v_e|^2 + \rho_0 gh \tag{16}$$

where ρ_0 is the reference density of the ambient water. Similarly, the internal pressure at the opening is found as

$$p = -\frac{1}{2}\rho_1|w|^2 + \rho_1 g(h+\delta) \tag{17}$$

The outflow vertical velocity w_0 can now be found if we assume that the pressure at the centreline of the forced plume at the opening is equal to the external pressure just outside the plume/jet. Hence,

$$w_0 = \sqrt{\frac{2gh(\rho_1 - \rho_0) + 2\rho_1 g\delta}{\rho_1 - \alpha^2\rho_0}} \tag{18}$$

The discharged volume flux Q through the opening, i.e. the drainage rate when there is no supply of water into the containment, is then found as

$$Q = CAw_0 \tag{19}$$

where C is the discharge coefficient, $A = \pi a^2$ is the area of the opening and w_0 is the outflow speed assumed uniform over the opening area. The discharge coefficient expresses the true volume flux relative to that from a uniform flow velocity over the cross-section of the opening. There are several physical effects influencing the discharge (Grose (1983)) and for the present case it is reasonable to split the discharge coefficient in two independent factors, namely the contraction coefficient C_c and the viscous correction coefficient C_v such that

$$C = C_c C_v \tag{20}$$

The flow out from an orifice into an ambient fluid accelerates through the orifice due to the change in pressure from the reservoir to the ambient. The point along the axis of the discharged flow where the pressure equals the ambient pressure is located outside the orifice and is known as the *vena contracta* (Lamb (1916)). This is where the cross-sectional area of the discharged jet has its minimum and where the flow velocity is known from Eq. (18). The cross-sectional area of the jet at the vena contracta relative to the orifice area is given by the contraction coefficient, which can be found from potential flow theory for inviscid flow. A classical result for 2D orifice flow in an infinite plane is $C_c = 0.611$ (see e.g. Lamb (1916)), while for 3D axisymmetric orifice flow the contraction coefficient takes the value $C_c = 0.5858$

(Grose (1985)). The viscous correction coefficient depends on the discharge Reynolds number $\mathrm{Rn}_d = (w_0 d)/\nu$, where d is the opening diameter and ν is the kinematic viscosity coefficient, and has the limiting value $C_v = 1$ when $Rn_d \to \infty$. Values of C_v for low and moderate Reynolds number orifice flows obtained from numerical solutions of the Reynolds-averaged Navier-Stokes equations were presented by Hollingshead et al. (2011), which shows that $C_v > 1$ for $\mathrm{Rn}_d > 14$. Further, C_v has the maximum value close to 1.25 when $Rn_d \approx 200$. This is also consistent with numerical results by Dabiri et al. (2008). In the present numerical study we consider axisymmetric discharge flow in full scale conditions characterized by high Reynolds number flow ($\mathrm{Rn} = \mathcal{O}(10^6)$), for which the viscous correction factor is found to be $C_v = 1.04$ from Hollingshead et al. (2011). Then the discharge coefficient used in the simulations becomes $C = C_c C_v = 0.61$.

A quasi static assumption is applied for the continuity of the contained water, such that the difference between the available bag volume and the instantaneous volume of contained water is balanced by $A_{wp}\delta$, where $A_{wp}(t)$ is the instantaneous water-plane area inside the bag and $\delta(t)$ is the instantaneous internal water level.

2.4. Hydrodynamic load model

A simplified hydrodynamic load model is developed, based on potential flow theory. When the cage start to drain, the structure will begin to shrink due to mass conservation and pressure difference across the tarpaulin. The shrinking also means that the external water is set into motion. We apply potential flow theory to model this effect and assume accelerations of the deformation are small compared to the gravity acceleration, such that no waves are generated at the free surface. This means we can consider the double body obtained by mirroring the hemispherical cage model across the free surface. Hence, we obtain the hydrodynamic problem of the flow induced by dilatation of a sphere in infinite fluid. Far away from the structure, the flow induced by the shrinking, or dilatation, then appear as that induced by a potential sink. We assume that potential flow theory applies in the external fluid domain, where also the jet/plume region along the z-axis is excluded, to study the hydrodynamic forces associated with dilatation of the sphere. We place a potential (negative) source at the centre of the double body, which has the velocity potential

$$\phi = \frac{m}{4\pi r} \tag{21}$$

where m is the source strength and $r = \sqrt{x^2 + y^2 + z^2}$ is the vector from the source at the origin to the field point (x, y, z). We define $R(t)$ to be the

instantaneous radius of the shrinking sphere. The source strength is found from the body boundary condition

$$\frac{\partial \phi}{\partial r}|_{r=R} = v_R \tag{22}$$

where v_R is the radial velocity of the cage surface due to dilatation of the cage. We have assumed that $v_R = \mathrm{d}R/\mathrm{d}t$ is uniform, i.e. only a function of time. This yields

$$\phi = v_R \frac{R^2}{r} \tag{23}$$

The external hydrodynamic pressure on the cage is then found from Bernoulli's equation,

$$p = -\rho_0 \frac{\partial \phi}{\partial t} + \frac{1}{2}\rho_0 \left| \frac{\partial \phi}{\partial r} \right|^2, \quad r = R \tag{24}$$

$$p = -\rho_0 R\ddot{R} - \rho_0 \frac{3}{2}\dot{R}^2, \tag{25}$$

where we have used

$$\frac{\partial \phi}{\partial t} = \ddot{R}R + 2\dot{R}^2, \qquad \frac{\partial \phi}{\partial r} = v_R. \tag{26}$$

This is similar to the dynamic pressure developed during collapse of a bubble, as derived by Rayleigh (1917). The resulting hydrodynamic forces are found by integration of the hydrodynamic pressure over the hemisphere with surface area $S = 2\pi R^2$, as

$$F = -\rho_0 2\pi R^3 \dot{v}_R - \rho_0 3\pi R^2 v_R^2 \tag{27}$$

This means the added mass $A_{rr} = \rho_0 2\pi R^3$ and quadratic damping $B_{rr} = \rho_0 3\pi R^2$ from external pressure due to the dilatation. The added mass and damping forces are distributed uniformly of the external bag surface area. The internal pressure distribution is found from Eq. (12) based on the instantaneous value of δ.

The hydrodynamic attraction force of the plume due to entrainment of surrounding water and continuity fluid mass, can be modelled by a distribution of two-dimensional (2D) potential sinks (negative potential sources) along the centreline of the plume. The strength of the sink can be found from a strip theory approach by requiring the induced radial velocity at the boarder b of the plume is equal to the entrainment velocity $v_e = \alpha w_m$. Hence, 2D external velocity potential is

$$\phi_{jet}(\xi) = b\alpha w_s \ln \xi, \quad \xi > a \tag{28}$$

The induced hydrodynamic pressure at the bottom of the cage is found from Bernoulli's equation

$$p(r) = -\frac{1}{2}\rho_0 \left|\frac{\partial \phi}{\partial \xi}\right|^2 = -\frac{1}{2}\rho_0 \left(\frac{b\alpha w_s}{\xi}\right)^2 \tag{29}$$

The induced hydrodynamic pressure is at most 1 % of the hydrostatic pressure difference across the bottom of the cage.

Similar as for the external flow, the flow through the orifice appear as a sink located at the centre of the circular opening. However, the strength of the sink is larger as that for the outside flow. As the outside flow external to the jet is due to entrainment from the ambient fluid, the internal flow due to the drainage is represented by a potential source (sink) at the centre of the orifice with strength

$$Q_0 = -2w_s A C_v \tag{30}$$

where w_s is the outflow velocity, $A = \pi a^2$ is the opening area of the orifice and C_v is the contraction coefficient. Hence, with $m = Q_0$ in Eq. (21) the velocity potential of the source reads

$$\phi = -\frac{a^2 C_v w_s(t)}{2r} \tag{31}$$

The internal hydrodynamic pressure is then

$$p(r) = -\rho_1 \frac{\partial \phi}{\partial t} - \frac{1}{2}\rho_1 \left|\frac{\partial \phi}{\partial r}\right|^2 = -\rho_1 \frac{a^2 C_v \dot{w}_s}{2r} - \frac{1}{8}\rho_1 \left(C_v w_s\right)^2 \left(\frac{a}{r}\right)^4 \tag{32}$$

2.5. Numerical simulation procedure

Figure 4 shows a flow chart of the numerical simulation procedure, in which the above-mentioned structural, discharge and hydrodynamic load models are implemented and the HHT-α method (Hughes (1983)) is used for numerical integration. The HHT-α method adopts the finite difference equations of the well-known Newmark-β method. The equations of motion are modified, however, using a parameter α, which represents a numerical lag in the damping, stiffness, nonlinear, and external forces. In a range of specified parameters, the HHT-α method is at least second-order accurate and unconditionally stable. It is useful in structural dynamics simulations incorporating large degrees of freedom, and in which it is desirable to numerically attenuate (or dampen-out) the response at high frequencies (Gavin (2016)). To solve the fluid-structure interaction problem an iterative process is adopted. At each simulation time step, the hydrodynamic pressure including added mass and damping forces acting on the finite elements and the

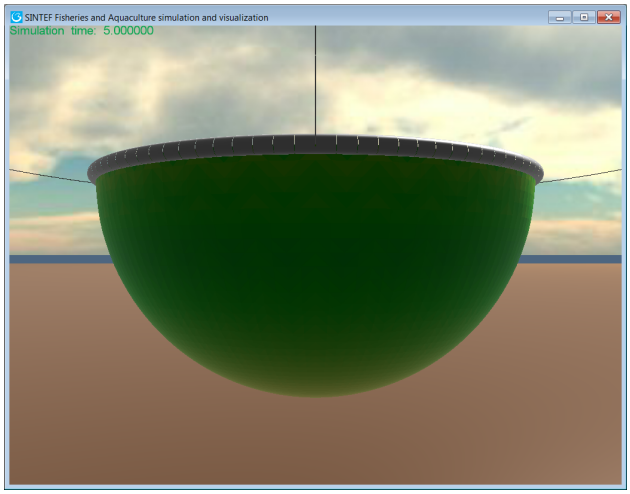

Figure 3: Numerical setup in FhSim.

nodal displacements are all taken as unknowns, considering that the internal water level, outflow velocity and structural deformation are interdependent. Iterations are performed until the relative deviations of nodal displacements are below a tolerance value which is set to be 10^{-3} in the present simulations. The calculated nodal displacements, volume change, internal water level and outflow velocity can be written to an output file at each simulation time step. Stress distributions among the finite elements can also be output from the simulation, and some benchmark analyses have been carried out with respect to the numerical accuracy and convergence behaviour of the FE structural model. The present numerical setup as shown in Fig. 3 is according to the physical experiments introduced below. The floating collar and the mooring lines are modeled by dedicated simulation objects in FhSim. They are connected to the flexible cage model with coupled dynamics. The bag material in the simulations resembles that typically used for closed cages in full scale, which is a PVC-coated fabric material. The material properties were obtained by tensile testing. As the material properties are anisotropic and dependent on the orientation of the reinforcement, different elasticity is obtained for different directions. This anisotriopic effect is not included in the numerical model, and directional averaged values of Young's modulus and the Poisson ratio is applied. The averaged Young's modulus was found to be 443 MPa, while Poisson's ratio was 0.3.

2.6. Physical experiments

Scaled physical model tests of the drainage process of a floating closed flexible cage was performed in a small tank filled with sea water. By adjusting

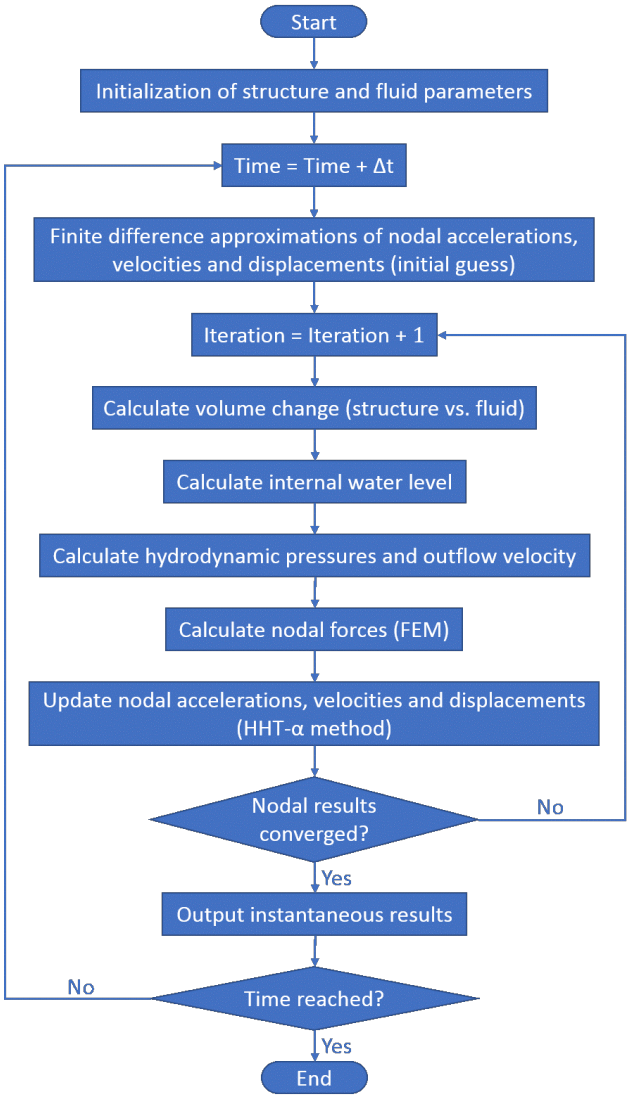

Figure 4: Flowchart showing the numerical simulation procedure.

the salinity of the water pumped into the cage model, different water densities inside and outside the cage were obtained. Drainage was initiated from an opening at the bottom of the cage. Three density differences were sought tested that corresponds to small, intermediate and large density differences for typical fjord locations.

A scaled physical model of a generic flexible closed cage structure was created with model scale 1 : 37.5. The model geometry was a hemisphere with diameter $D = 0.76$ m. The model depth h corresponded to the radius, i.e. $h = D/2$, as presented in Fig. 2. Cage displacement at 100 % fill ratio is then $V = \pi D^3/12 = 0.115\,\mathrm{m}^3$. The cage model was made of parachute watertight fabric (0-P) and mounted to a flexible floating collar. The collar was made of a PE plastic tube with outer pipe diameter $c = 0.023$ m, wrapped into a torus with diameter $D + c = 0.79$ m, providing sufficient buoyancy to balance the weight of the heavier water inside the cage at 100 % filling. Four mooring lines were applied to keep the cage model centered in the tank. The mooring lines were oriented with a small angle relative to the water plane and attached to the floating collar with even separation. A circular opening with diameter $2a = 0.02$ m was made with center at the bottom pole of the hemispherical cage model to study gravity driven drainage of the model. The opening was covered with a removable sheet of fabric during filling of the model, and the test was started by removing the sheet.

The tests were conducted at hydrostatic conditions in a tank with a diameter of 2.3 m and 1 m depth containing seawater with temperature of 9° C and salinity of approximately 34 ppt. This yields a water density of approximately $1026.4\,\mathrm{kg/m}^3$ according to the International one-atmosphere equation of state of seawater (Millero and Poisson (1981)), also known as the UNESCO equation of state. Water temperature and salinity in the tank were controlled before each test. Salinity inside and outside the cage at different depths were also measured during and at the end of the tests. After each test, the water in the tank was replaced before a new test was started. The sought mass density of the water inside the cage was obtained by mixing salt (NaCl) with seawater in a separate container. When the sought salinity and hence density was obtained, the water was pumped into the cage model with a calibrated impeller pump to keep control of the amount of water pumped into the model. Monitoring of the draining process was performed by adding dye inside the containment system and videotaping the surrounding water. The salinity of the internal water volume was monitored with conductivity sensors to be able to identify leakage of brackish water from the outside.

The density inside and outside the cage were then obtained from UNESCO equation of state with the measured salinity S_A and water temperature T. The time to drain the model (T_{drain}) was taken as the time interval

from removal of the fabric sheet that covered the opening, until the time where the drainage process stopped.

2.7. Image processing

Video recordings of the drainage process in the physical experiments were processed to track the bag contours with time. OpenCV (Open Source Computer Vision Library)[2] were utilized through its python API for this purpose. Images from the video streams were then analyzed, frame by frame. The image processing procedure consisted of six steps. First, the image was cropped to contain the bag only, while masking with filled rectangles was applied to remove background edges and details. Second step was to convert the image to gray-scale. Third step was to blur the image to smooth edges, which makes contour detection more robust. This was done using the Gaussian blur filter provided in the library. Fourth, the image was converted to binary black and white, using a given threshold of the gray-scale. The threshold value had to be tuned to properly separate the bag from the background. The fifth step consisted of eroding and dilating the image to remove noise, using the *erode* and *dilate* library functions. The sixth and final step was to find the contours in the image with the *findContours* library function and to identify the bag contour among all the returned contours of the image. The bag contour was found as the returned contour with the largest enclosed area. Collecting bag contours from each video frame, a time series of the bag contour deformation was obtained. From the contours, a time-series of the vertical motion of the bag's bottom was extracted. Since no calibration was performed in the experiment to relate pixel size to physical length at the plane of interest, the obtained time-series of bag contours must be taken as qualitative results. However, an attempt to relate pixel size to physical length for the bag contours was made using the known size of the bottom circular piece of the bag structure by measuring the horizontal distance between the seams at the bag's bottom. It is assumed that the same calibration also applies for the vertical direction in the middle region of the image.

3. Results

3.1. Scaled physical experiments

Scaled model tests with drainage of a closed flexible fish cage was conducted as described in section 2.6. Measured initial water conditions in the tank exterior to the cage and inside the cage and the resulting drainage time for the different tests are presented in Table 1.

[2]http://www.opencv.org

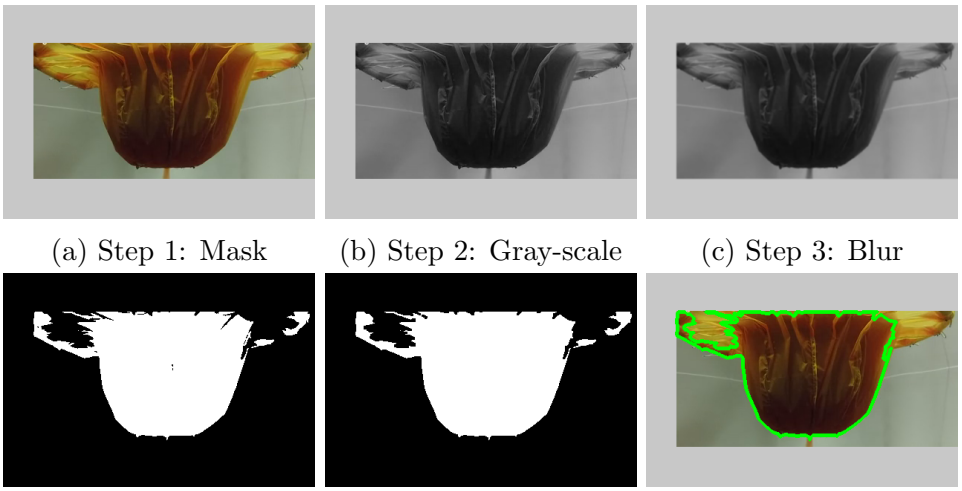

(a) Step 1: Mask (b) Step 2: Gray-scale (c) Step 3: Blur

(d) Step 4: Binary (e) Step 5: Dilate, erode (f) Step 6: Contour

Figure 5: Output from each step of the image processing procedure applied on video recording from Test 8 of the model experiment.

Table 1: Measured salinity and temperature of water outside and inside the cage model and resulting density difference and drainage time (model scale).

Test no.	External water prop.			Internal water prop.			V_0	$\Delta\rho$	T_{drain}
	$S_A^{(ext.)}$ [ppt]	$T_0^{(ext.)}$ [°C]	$\rho_0^{(ext.)}$ [kg/m^3]	$S_A^{(int.)}$ [ppt]	$T_0^{(int.)}$ [°C]	$\rho_1^{(int.)}$ [kg/m^3]	[m^3]	[kg/m^3]	[min]
8	33.97	8.8	1026.49	42.92	11.3	1032.98	0.115	6.49	66
9	34.07	8.8	1026.57	39.40	10.2	1030.42	0.112	3.85	88
10	33.91	8.8	1026.44	39.46	12.3	1030.09	0.111	3.64	93
12	34.30	8.8	1026.70	35.92	11.7	1027.52	0.111	0.824	280
13	34.19	9.0	1026.51	42.85	10.9	1033.12	0.111	6.61	68
14	34.23	8.9	1026.70	42.85	11.7	1032.93	0.111	6.23	67

Figure 6: Snap-shot from test no. 8. Outflow appear as an axisymmetric turbulent jet. A small inclination angle of the discharged plume relative to the vertical was observed.

Table 2: Estimated model scale flow parameters based on measured density differences of the drainage experiments. $At = (\rho_1 - \rho_0)/(\rho_1 + \rho_0)$ is the Atwood number, w_0 is the initial discharge velocity obtained from Eq. (18) with $\delta = 0$ and $h = D/2$, Fn is densimetric Froude number and Rn $= 2aw_0/\nu$ is the discharge Reynolds number.

Test no.	At	w_0 [m/s]	Fn	Rn
8	3.15E-03	0.22	1.41	4.3E+03
9	1.87E-03	0.17	1.41	3.3E+03
10	1.77E-03	0.16	1.41	3.3E+03
12	3.99E-04	0.08	1.41	1.5E+03
13	3.21E-03	0.22	1.41	4.4E+03
14	3.02E-03	0.21	1.41	4.2E+03

Immediately after removal of the fabric cover of the opening, the cage model started to drain. The bag was then moving slightly due to impact from the cover removal and by adjusting the bag position to the middle of the tank. This induced lateral motions of the bag that affected the outflow for the initial 3 minutes after start-up. After the transient start-up of the flow the outflow appeared as an axisymmetric turbulent jet (Figure 6). The tests were stopped when the discharge volume flux had a sudden decrease and the shape of the cage model seemed to reach a steady state, although the model did not drain completely and small leakage could still be observed. Based on density differences deduced from the measured water properties in Table 1, an estimate of the initial discharge velocity for the scaled model was obtained from Eq. (18) for each test. Non-dimensional flow parameters based on the measured densities and estimated initial outflow velocities are given in Table 2.

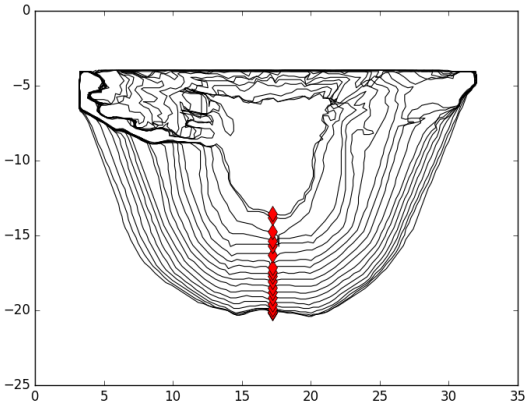

Figure 7: Bag contours from test 8 of the model experiment, plotted for every 3.5 min (model scale). The location of the discharge opening is highlighted with red markers.

3.1.1. Bag contours

Bag contours for given time instances were obtained from image processing of the video streams from the experiments, as outlined in Sec. 2.7. Resulting contours from test 8 characterized by large density difference are presented in Fig. 7. The time interval between each contour is 3.5 minutes in model scale. The contours appear to include a minor part of the discharged plume at some time instants. Similarly, bag contours obtained form test 9 are presented in Fig. 8. Some contours are missing due to drop-out of the video stream for a time interval of approximately 15 minutes in model scale.

3.2. Numerical simulations

3.2.1. Mesh convergence study

A sensitivity study of the mesh was performed to find which mesh resolution of the structural model that is sufficient to obtain convergence of the simulated drainage time. The physical parameters used in the tests correspond to the conditions of test 8 from the physical expersiments (Table 1). Computed drainage time for six different mesh resolutions are presented in Figure 9. Based on these results, the second finest mesh corresponding to the snapshot in the middle of Figure 9 was used for the rest of the simulations.

3.2.2. Case 1: Large density difference

The numerical model was applied to simulate drainage for large density difference in full scale, with conditions from Test 8 of the experiments given in Table 1 converted to full-scale by means of Froude scaling. An initial stage

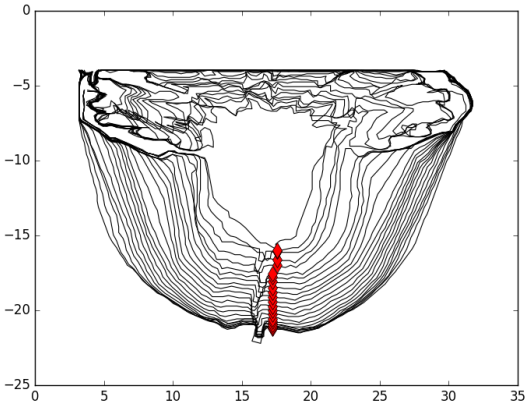

Figure 8: Bag contours from test 9 of the model experiment, plotted for every 3.5 min (model scale). The location of the discharge opening is highlighted with red markers.

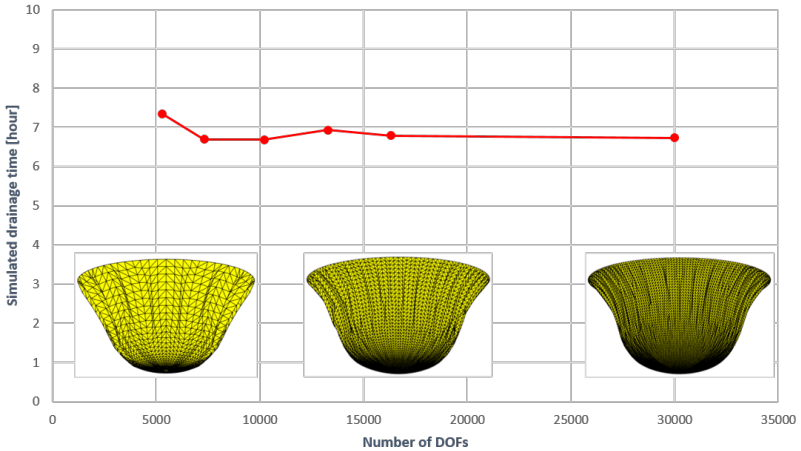

Figure 9: Convergence study of simulated drainage time relative to mesh resolution of the structural model. Conditions from test 8 of the physical experiments were applied.

of duration 30 min (simulated time in full scale) was included in the time simulation to find the equilibrium state of the cage, floater and mooring lines before the discharge was started. The drainage time was taken as the time duration from initiation of the discharge to the time instant when the outflow velocity reached zero. Time-histories of the vertical position of the cage top and bottom obtained from numerical simulation are presented in Fig. 10. Vertical position of the cage bottom obtained from image processing is also presented, with the initial vertical bottom position from the numerical model as the starting point. This is because the image processing results are just relative motions and not absolute values of position due to lack of a fixed reference point. Time series of the computed water level inside the cage relative to the ambient water level and the corresponding outflow velocity is shown in Figure 11. The computed internal water level has a rapid decay at the beginning of the drainage process, until about 2,4 hrs simulated time which means 1,9 hrs after startup of the discharge. The discharge velocity is also observed to decay rapidly just after drainage is initiated (Figure 11). Figure 12 shows the simulated time-history of the contained water volume and the cage volume during the discharge process. The cage model did not drain completely in the simulation and when the drainage process stopped, the remaining volume of water in the cage was about 9 % of the initial volume. In Figure 13, time lapse of the cage deformation obtained from the numerical simulation is compared with corresponding images of the video recordings from Test 8 of the physical experiments.

3.2.3. Case 2: Moderate density difference

Simulation with test conditions characterized by intermediate density difference between the contained water and the ambient, corresponding to Test 9 of the experiments, was performed. The obtained motions of the top and bottom point of the cage are presented in Figure 14, which show similar trends as the results of Case 1 (Fig. 10). The simulated motions of the cage bottom also show good agreement with the experimental results obtained from image processing (for both Case 1 and Case 2). However, these comparisons can only be taken as in a qualitative manner. The computed time series of the internal water level and discharge velocity (Figure 15) had also similar shape as that for Case 1 (Test ID 8) with large density difference. Time history of the contained water volume and cage volume are presented in Figure 16.

3.2.4. Case 3: Low density difference

When simulation of the case with low density difference was performed (test condition 12), the drainage process stopped when the cage volume was

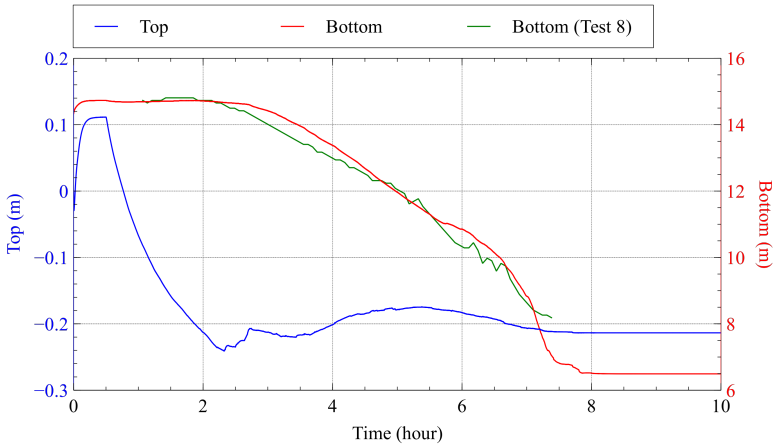

Figure 10: Time-history of the vertical position of the cage top and bottom obtained from numerical simulation in full scale of test 8 (large density difference). Vertical position of cage bottom obtained from image processing of video from the experiment test 8 is also presented with the initial vertical bottom position from the numerical model as the starting point, as the image processing only yielded relative motion.

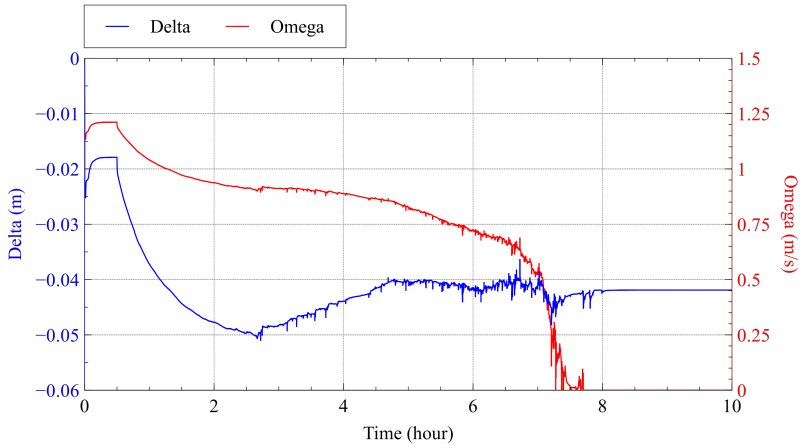

Figure 11: Time-history of the evolution of internal water level and the full-scale discharge velocity from numerical simulation of test 8 (large density difference).

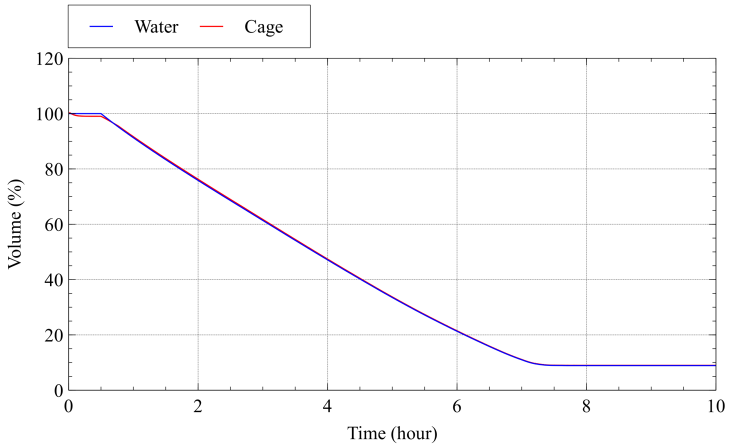

Figure 12: Computed time history of the cage volume and the contained water volume for test 8 (large density difference).

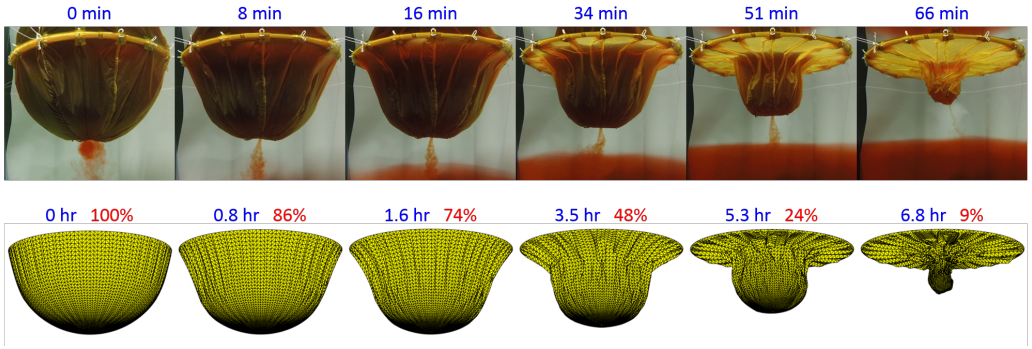

Figure 13: Time lapse of cage deformation from experiment test 8 compared with results from numerical simulation model. The simulation is performed with full scale dimensions. Measured drainage time of 66 min from physical experiments corresponds to 6.7 hours in full scale (Froude scaling).

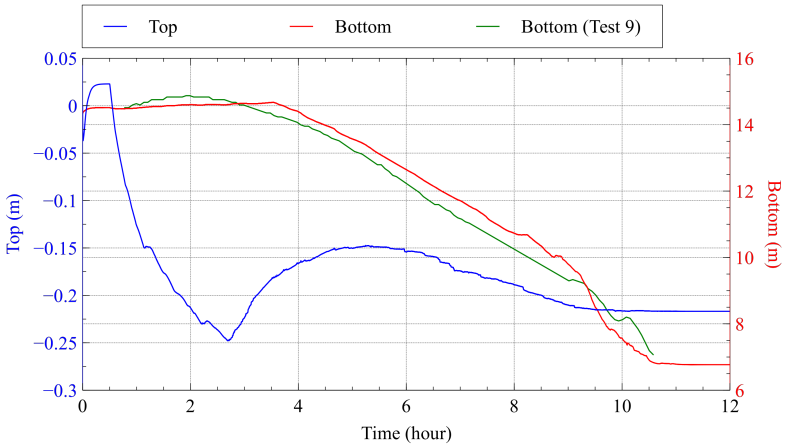

Figure 14: Time-history of the vertical position of the cage top and bottom from numerical simulation in full scale of test 9 (intermediate density difference). Vertical position of cage bottom obtained from image processing of video from the experiment test 9 is also presented with the initial vertical bottom position from the numerical model as the starting point, as the image processing only yielded relative motion.

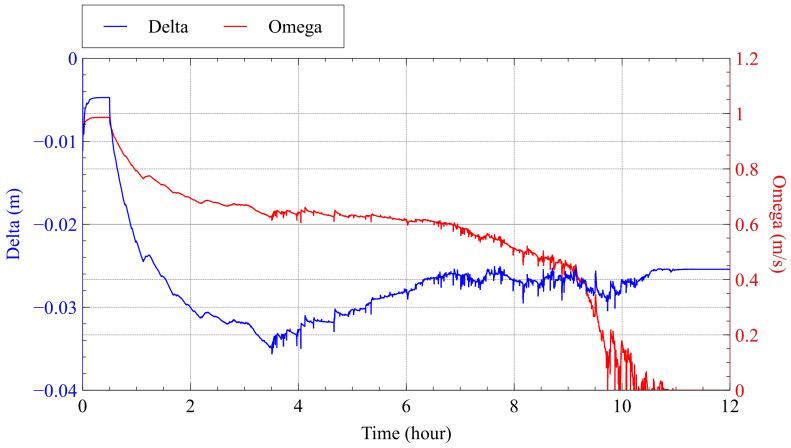

Figure 15: Time-history of the evolution of internal water level and the full-scale discharge velocity from numerical simulation of test 9 (intermediate density difference).

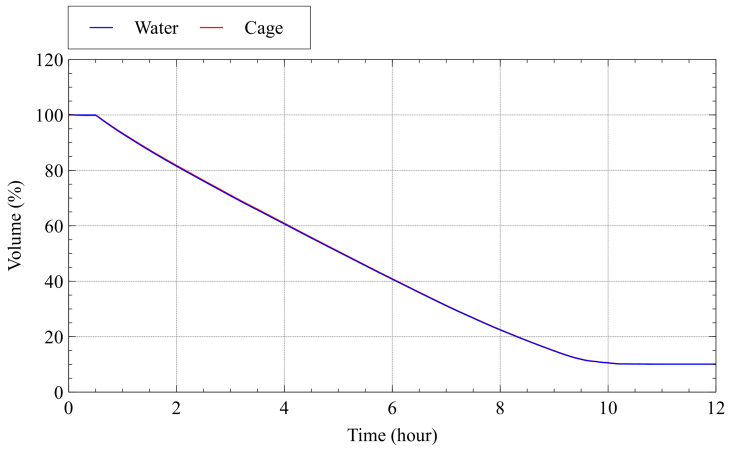

Figure 16: Computed time history of the cage volume and the contained water volume for test 9 (intermediate density difference).

reduced to about 91 % of the initial volume after about 3.3 hrs (Figure 17).

3.2.5. Case 4: Stratified density difference

Simulation of a case when there is a density difference inside and outside the bag only for the upper half depth of the bag, while the densities inside and outside the bag is equal for lower half depth. Hence, the density outside the bag at the drainage opening is equal to the density inside the bag. Figure 19 shows that the computed time series of the outflow velocity follows the evolution of the relative water level between the inside and the outside of the structure until about 18 hrs of simulated time. Computed vertical motions of the cage top and bottom are presented in Fig. 18, while computed time series of the cage volume and volume of contained water are shown in Fig. 20.

4. Discussion

4.1. The drainage process

The drainage process of the bag, as observed in the physical experiments, can be divided into three stages characterized by different physical effects and deformed bag geometries (see Fig. 13). We define the first stage (S1) to be the time interval from startup of the discharge to when the bag is starting to lay flat in the free surface and hence influence the free surface area inside the cage. This marks the start of the second stage (S2). The third and final stage (S3) starts when the free surface area inside the cage

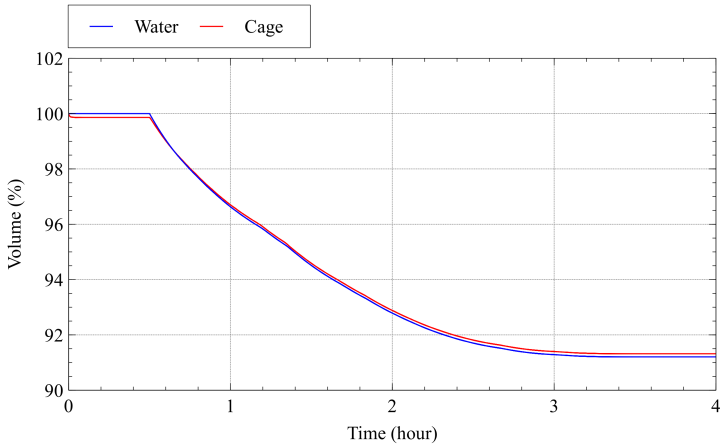

Figure 17: Computed time history of the cage volume and the contained water volume for test 12.

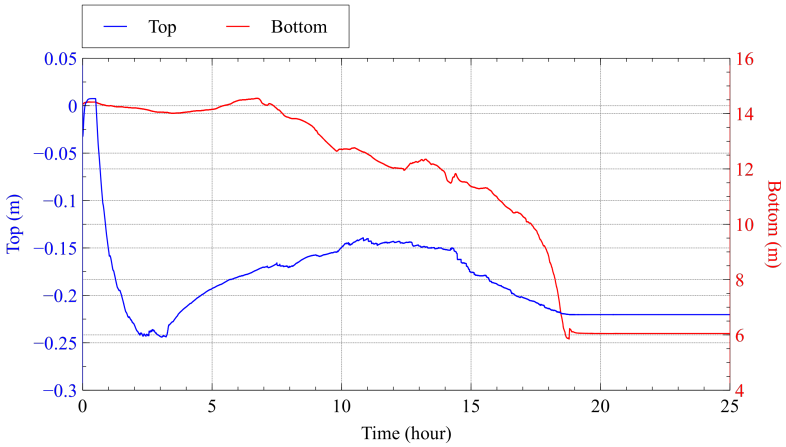

Figure 18: Time-history of the vertical position of the cage top and bottom from numerical simulation in full scale for case with stratified density condition of the ambient water. The lighter (brackish) water layer is from the free surface to half the depth of the cage.

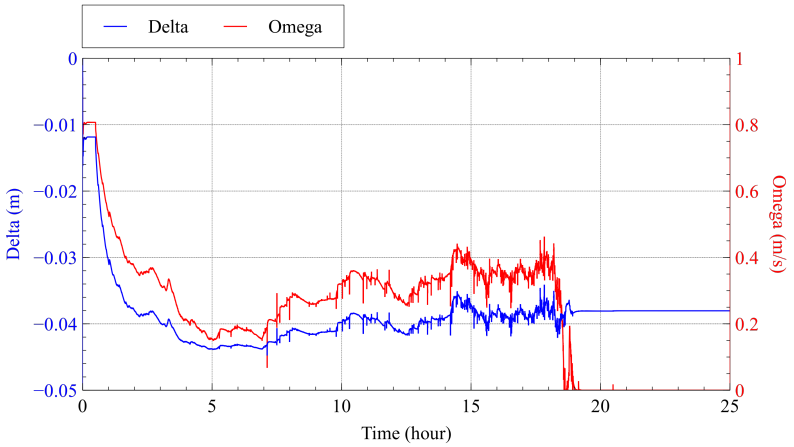

Figure 19: Time-history of the evolution of internal water level and the full-scale discharge velocity from numerical simulation of case with stratified density condition of the ambient water. The lighter (brackish) water layer is from the free surface to half the depth of the cage.

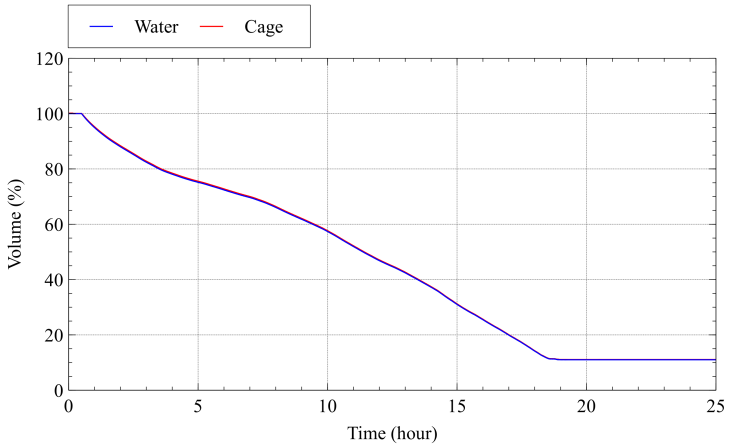

Figure 20: Computed time history of the cage volume and the contained water volume for case with stratified density condition of the ambient water. The lighter (brackish) water layer is from the free surface to half the depth of the cage.

narrow down and becomes smaller than the largest horizontal cross-section area of the submerged bag structure. S3 ends when the discharge stops.

Consider simulation Case I (large density difference). The discharge is started at time $t = 0.5$ hrs after the simulation model has reached initial equilibrium. During S1, the internal free surface area is constant and defined by the cage diameter. Further, discharge of the contained water makes the water level δ inside the bag sink rapidly while the top rim of the bag is lifted up due to the weight reduction and the buoyancy of the floating collar. The discharge velocity shows a similar decay trend as the internal water level during S1, which is reasonable as the hydrostatic pressure difference forcing the discharge is reduced. At the end of S1, the internal water level δ (Delta) reaches its minimum value (see e.g. Fig. 11). For case I, this occurs at time $t \approx 2.4$ hrs (1.9 hrs after start of the discharge) and when the contained water volume has reached 70% of the initial value. Going from S1 to S2, there is a change of trends of the top an bottom motions (Fig. 10) as well as the internal water level and discharge velocity (Fig. 11). However, while the discharge velocity continues to decay, the internal water level starts to increase. As the contained water is still being discharged, the increasing δ must be explained by increased deformations of the bag. The reduction of internal water-plane area A_{wp} during S2 makes the parameter δ more sensitive to the bag deformations, as the difference between the contained water volume and the instantaneous bag volume is balanced by $A_{wp}\delta$ in the applied quasi-static approach for the internal flow. This is a source to numerical noise in the computed time-series in Figs. 10 and 11 during complex deformations with buckling and folding of the bag structure. The final stage of the process (S3) starts at $t \approx 5$ hrs and is characterized by collapse of the bag. This includes complex fluid-structure interaction as well as contact and interaction between different parts of the bag structure, which are not adequately modeled with the present numerical model. The numerical noise is more pronounced in S3 where the bag undergoes large deformations while the free surface area as well as the volume of contained water is small. A sudden decay of the discharge velocity is seen at the end of S3, where the discharge finally stops. This is due to the rapid vertical motion of cage bottom at the end, which was also observed in the physical experiments. The time history of the contained water volume and the cage volume show a nearly linear decay with time during the whole process as shown in Fig. 12. The slight convex curvature implies that the initial tangent of the volume decay curve can be used to give a conservative estimate of the drainage time.

The main effect of increased density difference between the contained water and the ambient, as observed in the experiments and supported by numerical simulations, is decreased drainage time. This is reasonable as the

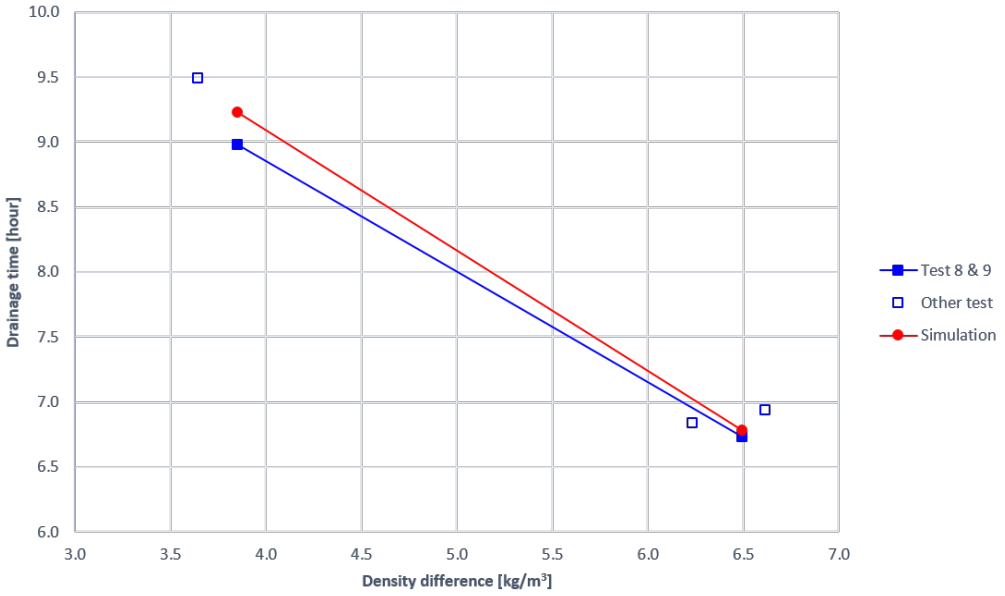

Figure 21: Comparison of the drainage time obtained from scaled physical experiments and from numerical simulations. Comparisons are made for Case 1 with large density difference and Case 2 with intermediate density difference. Froude-scaling is applied to convert drainage times from model scale to full scale values.

larger density difference implies an increased discharge velocity according to Eq. (18). Hence, the drainage process in simulation Case II (intermediate density difference) shows similar trends as in Case I (large density difference), but at a slower time-scale. Figure 21 shows a comparison of drainage times obtained from numerical simulation of Case I and II with measured drainage times for the corresponding cases of the scaled physical experiments. Froude scaling as defined in Eq. (14) is applied to convert measured drainage time from the scaled experiments to full scale. Simulation of case III with small density difference stopped when the water volume was reduced to 91 % of the initial volume, while in the physical experiments the bag drained completely. Small density difference means small hydrostatic pressure difference on either side of the tarpaulin such that the relative importance of the structural properties is larger compared to Cases I and II. Hence, the numerical results are more sensitive to mesh resolution of the bag structure for this case. However, a mesh convergence study is not performed for Case III as this case is less important from a design point of view, while the simulation time increases dramatically when the mesh is refined.

For the Cases I, II and III with uniform density of the ambient water, the difference in hydrostatic pressure on either side of the membrane structure

depends on the vertical position. Hence, the discharge velocity depends on the vertical position of the opening. This represent a nonlinearity which becomes increasingly important towards the end of the drainage process, when the bottom point of the bag and hence the discharge opening has the most rapid vertical motion (see Figs. 10 and 14).

The effects of density stratification of the ambient water was studied in simulation case IV. The ambient water was characterized by an upper layer of lighter water and a density jump at the depth equal to half the diameter of the hemispherical bag such that the density of the ambient water at the location of the discharge opening was equal to the contained water density. According to Eq. (18) the discharge velocity in the numerical model will not depend on the vertical position unless the opening moves into the region with lighter ambient water. This is why the discharge velocity is closely correlated to the internal water level δ (see Fig. 19), except for the final stage when the bottom of the bag reaches the layer of lighter water.

There is a scale effect of the discharge rate given by Eq. (19) due to Reynolds number dependence of the discharge coefficient through the viscous correction factor C_v. Numerical results by Dabiri et al. (2008) and Hollingshead et al. (2011) suggest that viscous effects are relevant for typical Reynolds numbers of the present model scale experiments (given in Tab. 2), while in full scale conditions this is small. This means that the drainage rate might be slightly larger in the scaled model tests than in full scale. Further, for the case of draining of a real closed flexible cage in the field, it is obvious that exposure to current and waves will influence the drainage process.

4.2. The numerical model

Based on a qualitative comparison, the numerical simulation model presented seems to reproduce the observed bag deformations from the experiments reasonably well. Quantitative comparisons made for the drainage time obtained with the numerical model with that measured in the scaled physical experiments shows good agreement. The initial equilibrium condition is not known a priori, but has to be obtained by iterations with the numerical model. This includes the static equilibrium shape of the flexible bag and hence the draft of the bag, as well as the initial internal water level relative to the external free surface. These are parameters governing the discharge velocity (Eq. (18)), which hence is not known in advance. The drainage rates related to the cage volume time histories shown in Figs. 12 and 16 appear to be close to constant with time, causing a nearly linear decay with time of the cage volume. This motivates attempts of simple hand-calculations. Conservative estimates of drainage times (about 67 - 68 % of measured values for tests 8 and 9) are obtained using the discharge velocity from Eq. (18)

with the ideal presumed initial conditions of zero internal surface elevation ($\delta = 0$) and hemispherical bag shape ($h = 0.5D$). The a priori unknown initial equilibrium conditions were found to be important for the resulting drainage times. The approximate representation of added mass and damping forces due to the bag deformation (Eq. (27)) that were deduced from dilatation of a sphere in infinite fluid, is quite crude but assumed to be adequate for the stages S1 and S2, while for S3 the deformed shape of the bag deviates significantly from a hemisphere which makes the approximation questionable. The added mass term is found to have minor effect on the drainage time, but it is relevant for the instantaneous responses and deformations of the structure. The structural model does not include contact detection, such that effects of contact between different parts of the bag structure that is likely to occur for large deformations (in particular during S3) is not modeled. This lack of physical constraints on the structural deformations due to contact can have effect on the simulated drainage process through erroneous estimates of bag volume, which in turn affects the estimates of internal water level and discharge velocity. The numerical model is still not considered to be fully validated. In particular, the time history of the internal free surface elevation obtained with the present numerical model needs to be validated. In the model presented, the internal free surface elevation has a direct impact on the discharge velocity and hence on the drainage time. On the other hand, the numerically obtained drainage times compare well with those measured in the experiments (cf. Fig. 21). Other uncertainties are related to the mooring lines, which tension were not measured in the experiments. Tension in the mooring lines could have had an impact on the global vertical motion of the bag, but this effect is assumed to be minor as the mooring lines were only lightly tightened and had a close to horizontal orientation..

4.3. Implications for design

From an operational point of view, it is important to detect drainage at an early stage such that countermeasures can be initiated. One solution can be to adjust the water exchange system to compensate for the leakage until a repair is possible. In light of the present numerical results, measurement of the internal water level or tension in the bag attachments to the floating collar would be the most sensible way do detect drainage (see Figs. 11 and 15). On the contrary, monitoring of the vertical position to the bottom of the cage, e.g. by an external pressure sensor, will not be efficient as the bottom does not move during the first stage of draining (S1, see Figs. 10 and 14). As drainage becomes critical for the fish before an eventually complete collapse of the cage, it is relevant to talk about the time to reach e.g. 50 % volume

reduction as a design criterion. Then, the present simulation model can be a relevant numerical tool in design of closed flexible cages.

5. Conclusion

Drainage of a water-filled floating flexible bag structure was studied by scaled physical experiments and numerical simulations. The drainage process was driven by gravity due to density difference between the contained water and the ambient, through a circular opening at the bottom of the hemispherical shaped bag. The problem has relevance for sea-based fish farming of Atlantic salmon in closed flexible containments at fjord locations, where density stratification may occur. Scaled physical experiments of the drainage process were conducted, where drainage time for several relevant density differences were measured. A new numerical simulation model was developed, coupling a FEM-based model for the structure with a simplified hydrodynamic load model based on potential flow theory combined with a dynamic model for the discharge of heavy water from the bag into the ambient. Qualitative comparison of the bag deformations are performed between images from video recordings of the experiments and snap-shots from numerical simulations, which shows satisfactory agreement. Good agreement is also found between the full scale equivalents of the measured drainage times from the scaled physical experiments and the drainage times obtained with the numerical model presented. Suggestions are made for early detection of drainage for closed flexible cages.

Acknowledgements

This work was financed by the Norwegian Fisheries and Aquaculture Research Fund (FHF) through grant 901287.

References

Batchelor, G. K., 1954. Heat convection and buoyancy effects in fluids. Quarterly Journal of the Royal Meteorological Society 80 (345), 339–358.
URL http://dx.doi.org/10.1002/qj.49708034504

Blevins, R., 2003. Applied fluid dynamics handbook. Van Nostrand Reinhold Co.
URL https://books.google.no/books?id=G-ZUAAAAMAAJ

Chen, X.-J., sheng Wu, Y., cheng Cui, W., Jensen, J. J., 2006. Review of hydroelasticity theories for global response of marine structures. Ocean

Engineering 33 (3), 439 – 457.
URL http://www.sciencedirect.com/science/article/pii/S002980180500154X

Dabiri, S., Sirignano, W. A., Joseph, D. D., 2008. Two-dimensional and axisymmetric viscous flow in apertures. Journal of Fluid Mechanics 605, 118.

Flores, F. G., Oate, E., 2005. Improvements in the membrane behaviour of the three node rotation-free bst shell triangle using an assumed strain approach. Computer Methods in Applied Mechanics and Engineering 194 (6), 907 – 932.
URL http://www.sciencedirect.com/science/article/pii/S004578250400307X

Flores, F. G., Oate, E., 2007. A rotation-free shell triangle for the analysis of kinked and branching shells. International Journal for Numerical Methods in Engineering 69 (7), 1521–1551.
URL http://dx.doi.org/10.1002/nme.1823

Gärdsback, M., Tibert, G., 2007. A comparison of rotation-free triangular shell elements for unstructured meshes. Computer Methods in Applied Mechanics and Engineering 196 (49), 5001 – 5015.
URL http://www.sciencedirect.com/science/article/pii/S0045782507002927

Gavin, H. P., 2016. Numerical integration in structural hydrodynamics. In: CEE 541. Structural Dynamics. Duke University, Department of Civil & Environmental Engineering.

Griffith, B. E., Luo, X., McQueen, D. M., Peskin, C. S., mar 2009. SIMULATING THE FLUID DYNAMICS OF NATURAL AND PROSTHETIC HEART VALVES USING THE IMMERSED BOUNDARY METHOD. International Journal of Applied Mechanics 01 (01), 137–177.

Grose, R. D., 1983. Orifice flow at low reynolds number. Journal of Pipelines 3, 207–214.

Grose, R. D., 1985. Orifice contraction coefficient for inviscid incompressible flow. Journal of Fluids Engineering 107, 36–43.

Hart, J. D., Peters, G., Schreurs, P., Baaijens, F., 2003. A three-dimensional computational analysis of fluidstructure interaction in the aortic valve. Journal of Biomechanics 36 (1), 103 – 112.

URL http://www.sciencedirect.com/science/article/pii/S0021929002002440

Hollingshead, C., Johnson, M., Barfuss, S., Spall, R., 2011. Discharge coefficient performance of venturi, standard concentric orifice plate, v-cone and wedge flow meters at low reynolds numbers. Journal of Petroleum Science and Engineering 78 (3), 559 – 566.
URL http://www.sciencedirect.com/science/article/pii/S0920410511001987

Hou, G., Wang, J., Layton, A., 2012. Numerical methods for fluid-structure interaction a review. Communications in Computational Physics 12 (2), 337377.

Hughes, T., 1983. Analysis of transient algorithms with particular reference to stability behavior. In: Computational Methods for Transient Analysis. Amsterdam, North-Holland, p. 67155.

Korobkin, A., Părău, E. I., Vanden-Broeck, J.-M., 2011. The mathematical challenges and modelling of hydroelasticity. Philosophical Transactions of the Royal Society of London A: Mathematical, Physical and Engineering Sciences 369 (1947), 2803–2812.
URL http://rsta.royalsocietypublishing.org/content/369/1947/2803

Lader, P., Fredriksson, D. W., Volent, Z., DeCew, J., Rosten, T., Strand, I., 2015. Drag forces on, and deformation of, closed flexible bags. Journal of Offshore Mechanics and Arctic Engineering 137 (4), 041202–041202–8.

Lader, P., Fredriksson, D. W., Volent, Z., DeCew, J., Rosten, T., Strand, I., 2017. Wave response of closed flexible bags. Journal of Offshore Mechanics and Arctic Engineering 139 (5), 051301–051301–9.

Lamb, H., 1916. Hydrodynamics. University Press.
URL https://books.google.no/books?id=OztMAAAAMAAJ

Løland, G., Aarsnes, J. V., 1994. Fabric as construction material for marine applications. In: Hydroelasticity in Marine Technology. Balkema, Rotterdam, Netherlands, pp. 275–286.

Millero, F. J., Poisson, A., 1981. International one-atmosphere equation of state of seawater. Deep Sea Research Part A. Oceanographic Research Papers 28 (6), 625 – 629.

URL http://www.sciencedirect.com/science/article/pii/0198014981901229

Morton, B. R., 1959. Forced plumes. Journal of Fluid Mechanics 5 (1), 151163.

Onate, E., Cervera, M., 1993. Derivation of thin plate bending elements with one degree of freedom per node: A simple three node triangle. Engineering Computations 10 (6), 543–561.
URL https://doi.org/10.1108/eb023924

Rayleigh, O., 1917. Viii. on the pressure developed in a liquid during the collapse of a spherical cavity. The London, Edinburgh, and Dublin Philosophical Magazine and Journal of Science 34 (200), 94–98.
URL http://dx.doi.org/10.1080/14786440808635681

Reite, K.-J., Føre, M., Aarsæther, K. G., Jensen, J., Rundtop, P., Kyllingstad, L. T., Endresen, P. C., Kristiansen, D., Johansen, V., Fredheim, A., 2014. Fhsim time domain simulation of marine systems. In: Proceedings of the 33rd International Conference on Ocean, Offshore and Arctic Engineering (OMAE 2014). No. 45509. ASME, San Francisco, CA, USA, p. V08AT06A014.
URL http://dx.doi.org/10.1115/OMAE2014-23165

Sabourin, F., Brunet, M., 2006. Detailed formulation of the rotationfree triangular element s3 for general purpose shell analysis. Engineering Computations 23 (5), 469–502.
URL https://doi.org/10.1108/02644400610671090

Solaas, F., Rudi, H., Berg, A., Tvinnereim, K., 1993. Floating fish farms with bag pens. In: Fish Farming Technology. Balkema, Rotterdam, Netherlands.

Strand, I., Srensen, A., Volent, Z., Lader, P., 2016. Experimental study of current forces and deformations on a half ellipsoidal closed flexible fish cage. Journal of Fluids and Structures 65 (Supplement C), 108 – 120.
URL http://www.sciencedirect.com/science/article/pii/S0889974616302857

Weinan, E., Engquist, B., Oct. 2003. Multiscale modeling and computation. Notices of the AMS 50 (9).